

## Article

# Inhibition of Zinc Dendrites Realized by a $\beta$ -P(VDF-TrFE) Nanofiber Layer in Aqueous Zn-Ion Batteries

Geumyong Park,<sup>1,†</sup> Hyeonghun Park,<sup>1,†</sup> WooJun Seol,<sup>2</sup> Seokho Suh,<sup>1</sup> Ji Young Jo,<sup>2</sup> Santosh Kumar,<sup>1,3,\*</sup> and Hyeong-Jin Kim,<sup>1,\*</sup>

<sup>1</sup> Graduate School of Energy Convergence, Institute of Integrated Technology, Gwangju Institute of Science and Technology (GIST), 123 Cheomdangwagi-ro, Buk-gu, Gwangju, 61005, Republic of Korea

<sup>2</sup> School of Materials Science and Engineering, Gwangju Institute of Science and Technology (GIST), 123 Cheomdangwagi-ro, Buk-gu, Gwangju, 61005, Republic of Korea

<sup>3</sup> Research Institute for Solar and Sustainable Energies (RISE), Gwangju Institute of Science and Technology (GIST), 123 Cheomdangwagi-ro, Buk-gu, Gwangju, 61005, Republic of Korea

\* Correspondence: [skumar@gist.ac.kr](mailto:skumar@gist.ac.kr) and [hjkim@gist.ac.kr](mailto:hjkim@gist.ac.kr)

<sup>†</sup> These authors have contributed equally to this work.

**Abstract:** Uncontrollable Zn dendrite formations and parasitic side reactions on Zn electrodes induce poor cycling stability and safety issues, preventing the large-scale commercialization of Zn-ion batteries. Herein, to achieve uniform Zn deposition and suppress side reactions, an electrospun ferroelectric poly(vinylidene fluoride-co-trifluoroethylene) copolymer, a [P(VDF-TrFE)] nanofiber layer, is introduced as an artificial solid-electrolyte interface on a Cu substrate acting as a current collector. The aligned molecular structure of  $\beta$ -P(VDF-TrFE) can effectively suppress localized current density on the Cu surface, lead to uniform Zn deposition, and suppress side reactions by preventing direct contact between electrodes and aqueous electrolytes. The half-cell configuration formed by the newly fabricated electrode can achieve an average coulombic efficiency of 99.2% over 300 cycles without short circuiting at a current density of 1 mA cm<sup>-2</sup> and areal capacity of 1 mAh cm<sup>-2</sup>. Stable cycling stability is also maintained for 200 cycles at a current density of 0.5 A g<sup>-1</sup> in a full-cell test using MnO<sub>2</sub> as a cathode.

**Keywords:** artificial interface; coulombic efficiency; electrospinning; MnO<sub>2</sub> Cathode; PVDF

## 1. Introduction

In recent years, due to environmental pollution, climate change, and the energy crisis, the demand for environmentally friendly energy storage devices with high performance has dramatically increased [1-4]. Since 1991, when the first commercial lithium-ion batteries (LIBs) were revealed, LIBs have dominated the energy storage market and various industrial applications due to their longevity and high energy density [5-7]. However, due to the high cost, toxicity, and flammability of LIBs, environmentally friendly and nonflammable aqueous alternatives to LIBs have attracted considerable interest [8-12]. Among the various types of aqueous batteries, Zn-ion batteries (ZIBs) have been intensely studied as next-generation energy storage devices due to their high specific capacity (825 mAh g<sup>-1</sup>), low redox potential (-0.76 V vs. SHE), high abundance of Zn metal and low costs [13-19]. However, Zn dendrite formation during battery operation can cause an internal short circuit and lead to severe problems in terms of cell performance and safety.

These dendrites are mainly formed by the accumulation of electric charges on the protrusion of the electrode to create a local current density, and the Zn ions are intensively electrodeposited at the same site, which is called the 'tip effect' [20]. In addition, parasitic side reactions such as the hydrogen evolution reaction (HER) and zinc hydroxide sulfate (ZHS) byproduct formation between the electrolyte and the electrode interface also adversely affect cell performance and safety [18]. Recently, the most popular strategy for mitigating localized current density and side reactions on Zn electrodes has been to introduce

an artificial interface between the electrode surface and the electrolyte [19, 21-24]. From the material aspect, polymers are suitable as artificial interface layers because they induce uniform Zn deposition through functional groups and offer better adhesion properties due to flexibility, which is advantageous in terms of electrode durability [25].

Poly(vinylidene fluoride) (PVDF) and its copolymer are known for their high dielectric constant ( $\epsilon_r \approx 10$  at 1 kHz), superior mechanical strength, thermal stability, and chemical resistance [26, 27]. In particular, highly polar  $\beta$ -crystalline phase PVDF-based polymers with all-trans conformations have outstanding ferroelectric properties among their various phases [28, 29]. As a result of the aligned structure,  $\beta$ -PVDF has the high dipole moments between the hydrogen and fluorine moieties, which are aligned almost perpendicular to the carbon axis, and when an external electric field above a certain intensity is applied, electric displacement occurs [30-32]. Ascribed to these unique characteristics of  $\beta$ -PVDF-based polymers, many recent articles have focused on their potential application in energy storage devices [33-37]. There have been several attempts to apply the characteristics of  $\beta$ -PVDF in LIBs and ZIBs. W. J. Song *et al.* demonstrated that  $\beta$ -PVDF could induce high-rate Li-ion diffusion [33]. C. Hwang *et al.* reported that  $\beta$ -PVDF effectively drives dense and uniform Li deposition [34]. Y. Wang *et al.* reported that modifying a typical Zn anode with a PVDF-based polymer can homogenize the current distribution and suppress parasitic side reactions on the Zn anode surface [38]. The critical point of these studies is that the intense polarization of  $\beta$ -PVDF on an electrode advantages metal ion diffusion during battery cycling. However, since the thermodynamically stable  $\alpha$ -phase is the dominant phase in raw PVDF materials, applying heat or an electric field is needed to form the  $\beta$ -phase from the  $\alpha$ -phase [30-32].

Herein, we apply a poly(vinylidene fluoride-co-trifluoroethylene) copolymer, a [P(VDF-TrFE)] nanofiber layer (PNF), to achieve a high  $\beta$ -crystalline fraction. The introduction of trifluoroethylene (TrFE) to copolymerize with PVDF can increase the fraction of the  $\beta$ -phase compared to pure PVDF, ascribed to the strong steric hindrance of fluorine atoms [39]. Additionally, electrospinning using a high applied voltage is an efficient technique for forming a high  $\beta$ -crystalline fraction and is able to provide a highly porous nanofiber layer, which enables facile electrolyte penetration into the layer [29, 40-43]. In our cell design, a uniform PNF layer is electrospun onto a Cu substrate acting as a current collector, which is known as a metal that has a high binding energy to  $\text{Zn}^{2+}$  ions [44]. As a result, during cell operation, the PNF layer acts as a passivation layer, and the oriented dipole moments vectors of the PNF along the localized electric field on the electrode surface effectively relieve the localized current density, thereby leading to uniform Zn deposition and achieving a superior cycle life under various current densities.

## 2. Experimental section

### 2.1. P(VDF-TrFE) and PVDF Nanofiber fabrication

The electrospinning solution containing 11 wt% P(VDF-TrFE) with MW = 450,000 g mol<sup>-1</sup> (70:30 mol %) was prepared by dissolving the polymer in a 60:40 weight ratio of N,N-dimethylformamide (DMF) and acetone under intense magnetic stirring for 3 hr at 50 °C. In addition, 1 wt.% pyridine formate buffer was added to the solution to increase the solution conductivity and to produce uniform and beadless nanofiber mats with an average fiber diameter of ~ 400 nm on copper foil wrapped over the drum collector. The thickness of the electrospun nanofiber layer was ~ 5  $\mu\text{m}$ . The as-prepared solution was fed into a 12 ml plastic syringe attached to a 23-gauge steel needle and pumped to a spinneret using a syringe pump with a flow rate of 0.5 mL/hr at 18 kV with a tip-to-collector distance (TCD) of 12 cm at 100 rpm. The as-spun nanofiber mat was annealed for 2 hr at 120 °C in a vacuum oven before use to enhance the high  $\beta$ -crystalline phase. To prepare the PVDF nanofiber layer, a similar operating procedure was followed except that 12 wt.% PVDF (Sigma Aldrich) with MW= 534,000 g mol<sup>-1</sup> was employed at an applied voltage of 23 kV, with a flow rate of 0.8 mL/hr and a TCD of 17 cm.

## 2.2. Preparation of $\text{MnO}_2$ electrode

The cathode slurry was prepared by mixing 70 wt%  $\text{MnO}_2$  (US Research Nano-material), 20 wt% Super C (MTI Co.), and 10 wt% PVDF (Solef 5130, Solvay). The slurry was cast on 30  $\mu\text{m}$  Ti foil by the doctor blade method with a loading density of 1.9–2.1  $\text{mg cm}^{-2}$ .

## 2.3. Cell assembly

The half cells were assembled using the Zn electrode and Zn@Cu or Zn@PNF-Cu electrode. Two M  $\text{ZnSO}_4$  (Ducksan) in deionized water was employed as the electrolyte, and glass fiber filter paper (Watman) was employed as the separator. The symmetric cells were assembled using two identical Zn@Cu or Zn@PNF-Cu electrodes with the same electrolyte. Zn (5  $\text{mAh cm}^{-2}$ ) was first deposited on Cu and PNF-Cu and cycled under various current densities with an areal capacity of 1  $\text{mAh cm}^{-2}$ . The full cells were assembled using a  $\text{MnO}_2$  cathode and Zn@Cu or Zn@PNF-Cu electrode. Then, 2 M  $\text{ZnSO}_4$  + 0.1 M  $\text{MnSO}_4$  (Daejung Chemicals & Metals Co.) in DI water was used as the electrolyte to reduce the  $\text{Mn}^{2+}$  dissolution of  $\text{MnO}_2$ . All the cells were assembled in an open atmosphere and kept at 25 °C for 24 h to allow electrolyte penetration after assembly.

## 2.4. Electrochemical measurements

All electrochemical measurements were conducted using a two-electrode system assembled in CR2032-type coin cells (U&S energy Co.). A galvanostatic battery cycler (WBCS 3000, Wonatech) was used to measure the cycling performance. The Zn plating/stripping process was conducted using a half cell. In the half-cell test, Zn was deposited onto the Cu electrode at 1  $\text{mA cm}^{-2}$  for an hour and stripped to 1 V at the same current density repeatedly. For long-cycle galvanostatic charge/discharge tests of symmetric cells and full cells, 5  $\text{mAh cm}^{-2}$  Zn was deposited onto Cu and PNF-Cu electrodes at 1  $\text{mA cm}^{-2}$  before cell assembly to provide a Zn source. Symmetric cells were charged/discharged under various current densities (0.1  $\text{mA cm}^{-2}$ , 1  $\text{mA cm}^{-2}$ , 5  $\text{mA cm}^{-2}$  and 10  $\text{mA cm}^{-2}$ ) with an areal capacity of 1  $\text{mA cm}^{-2}$ . The electrochemical performance of the full cells was evaluated in a voltage range between 0.8 V and 1.9 V at 0.5  $\text{A g}^{-1}$ . The LSV and CV measurements were carried out on a VSP-300 instrument (Biologic). LSV for the Tafel plot was conducted at a scan rate of 0.5  $\text{mV s}^{-1}$  with a voltage range from -0.1 V to 0.1 V. CV for the half cell test was conducted at a scan rate of 1  $\text{mV s}^{-1}$  with a voltage range from -0.2 V to 0.45 V. CV for the full-cell test was conducted at a scan rate of 0.1  $\text{mV s}^{-1}$  with a voltage range from 0.6 V to 1.8 V. Electrochemical impedance spectroscopy (EIS) measurements were conducted using a VSP-300 with an impedance frequency range of 100 kHz to 0.01 Hz and an alternating perturbation of  $\pm 10$  mV. All electrochemical measurements were carried out in a 25 °C thermostatic chamber.

## 2.5. Material characterization

The cycled cells were carefully disassembled for postcycling measurements. The electrodes were rinsed using deionized water to remove residual electrolyte, followed by drying using pressed air to prevent oxidation. After disassembly of the cells, the PNF layer is carefully removed to observe the morphology of the deposited Zn. The morphologies of the materials were observed using FE-SEM (JSM-7500F, JEOL) and EDS (Ultim Max 65, Oxford Instrument). XRD (Bruker, D8 Advance) with a  $\text{Cu K}\alpha$  radiation source and FTIR (Vertex 70, Bruker) were conducted to analyze the  $\beta$ -phase formation of the PNF layer. Contact angle measurement was executed to analyze the hydrophilicity of the electrodes using DI water at room temperature (25 °C). Electric field (P-E) hysteresis loops of the fabricated Pt/P(VDF-TrFE)/Cu capacitor were measured using a ferroelectric tester (Precision LC, Radiant Technology) with triangular pulses with an amplitude of 180 V and a frequency of 2.5 kHz.

### 3. Results and discussion

#### 3.1. Characterization of the PNF-Cu electrode

Cu foil was selected as the current collector for P(VDF-TrFE) electrospinning (PNF-Cu). Figure S1 in the Supporting Information (SI) shows the nucleation overpotentials of the Zn||Zn cell and Zn||Cu cell. When Zn ions are deposited on the Cu foil, they show a lower nucleation potential than when they are deposited on the Zn foil. This is due to the high binding energy between  $\text{Zn}^{2+}$  and Cu foil, suggesting that adopting a zincophilic Cu substrate can be an effective method to suppress Zn dendrite formation [34, 45]. Figure 1a shows the surface of bare Cu foil; grooves or protrusions are observed on the surface, which lead to the formation of dendrites by creating an environment where Zn ions can be intensively electrodeposited [46].

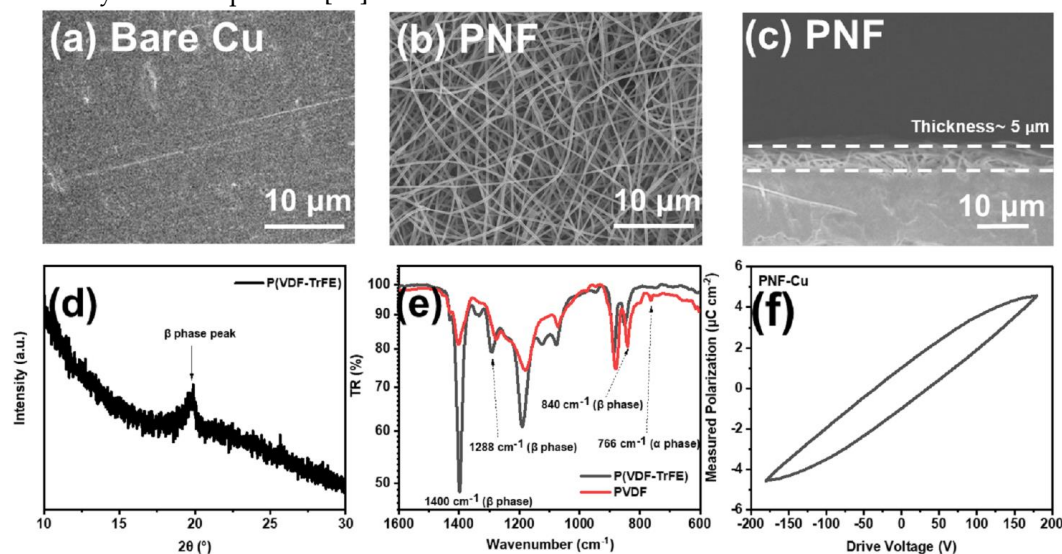


**Figure 1.** (a) Top-view SEM images of bare Cu foil and (b) PNF, (c) cross-sectional SEM image, (d) XRD pattern, (e) FT-IR spectra, and (f) hysteresis loop of PNF.

An electrospun PNF layer was introduced on the Cu foil surface to suppress dendrite formation, and Figure 1b and c show the morphology and thickness of the PNF layer, respectively. PNFs with a diameter of  $\sim 400$  nm and a layer thickness of  $\sim 5$   $\mu\text{m}$  were uniformly electrospun on the Cu substrate. To verify that the PNF layer has a crystalline  $\beta$ -phase for ferroelectricity, the  $\beta$ -phase crystallinity is determined using X-ray diffraction (XRD). Figure 1d shows the characteristic peak of  $\beta$ -P(VDF-TrFE), which is located at  $\sim 20^\circ$ , revealing that the crystalline  $\beta$ -phase of P(VDF-TrFE) is effectively formed [47]. To induce higher crystalline  $\beta$ -phase, heat treatment of the PNF layer was conducted at  $120^\circ\text{C}$  for 2 hr after the electrospinning process [45]. Equation 1 is used to calculate the  $\beta$ -phase content in the PNF layer through the FTIR spectra (Figure 1e) [48].

$$F(\beta) = \frac{A_\beta}{\left(\frac{K_\beta}{K_\alpha}\right)A_\alpha + A_\beta} \quad (1)$$

$F(\beta)$  -  $\beta$ -phase content,  $K_\alpha$ ,  $K_\beta$  - the absorption coefficient for each phase, which is  $7.7 \times 10^4$   $\text{cm}^2 \text{mol}^{-1}$  and  $6.1 \times 10^4$   $\text{cm}^2 \text{mol}^{-1}$ , respectively.  $A_\alpha$ ,  $A_\beta$  - the absorbance peaks of nonpolar  $\alpha$  and polar  $\beta$  phases at  $766$  and  $840$   $\text{cm}^{-1}$ , respectively.

The  $\beta$ -phase ratio of PNF was calculated to be 94%, which is generally higher than that when heat-treated in the form of a film, indicating that the  $\beta$ -phase was effectively generated through electrospinning [49,50]. On the other hand, the  $\beta$ -phase ratio of the electrospun PVDF nanofiber layer under a similar fabrication process was 83%, which shows the ease of  $\beta$ -phase formation of PNF due to the introduction of TrFE (Figure 1e). The polarization versus electric field (P-E) hysteresis loop in Figure 1f shows that the dielectric response of the PNF layer under an external electric field can limit the localized current density on the tip of the protrusion, which is a key factor in reducing the dendrite growth. When the external electric field is removed, very low remanent polarization is



observed ( $\approx 1.0 \mu\text{C cm}^{-2}$ ), which infers that it has a limited effect on increasing the over-potential during the cell operation.

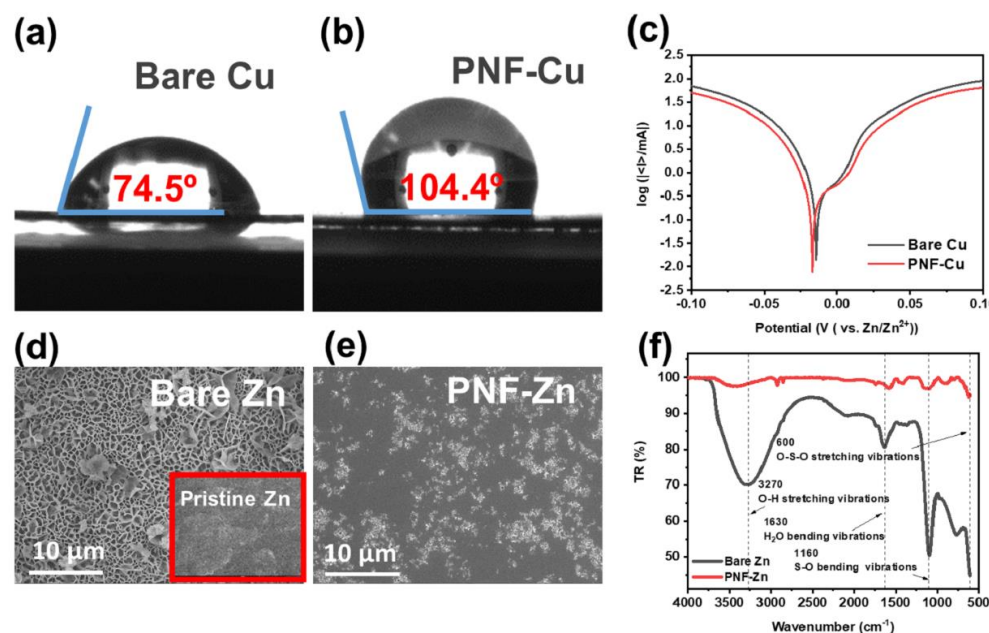


**Figure 2.** Contact angle measurement for aqueous solutions on (a) bare Cu, (b) PNF-Cu, (c) linear polarization curves showing the corrosion on bare Cu and PNF-Cu, Top-view SEM images of (d) bare Zn after immersion in the electrolyte for 7 days and pristine Zn (inset) (e) PNF-Zn after immersion in the electrolyte for 7 days, and (f) FTIR spectra of the bare Zn and PNF-Zn after immersion in the electrolyte for 7 days.

To check the compatibility with the electrolyte, contact angle and EIS measurements were conducted. The bare Cu substrate and PNF-Cu contact angles are 74.5° and 104.4°, respectively, as determined using deionized water (DI water) at room temperature (Figure 2a and b). The high contact angle of the PNF-Cu electrode is due to the hydrophobic properties of the PNF layer. The ionic conductivity of the PNF layer was measured by EIS measurements with a Cu symmetric cell and PNF-Cu symmetric cell (Figure S2 in SI). Despite the hydrophobic property of PNF, it exhibits an ionic conductivity of  $2.59 \times 10^{-2} \text{ S cm}^{-1}$ , which is large enough for Zn<sup>2+</sup> conduction, which is achieved due to the small thickness and porous structure of the PNF layer [19]. Since very thin PNF is introduced on the Cu foil, there is a very slight increase in the bulk resistance ( $R_b$ ). The steeper slope in the low-frequency region of the PNF-Cu electrode than that of the bare-Cu electrode indicates the capacitive response from the high dielectric constant of the P(VDF-TrFE), and polarity of the PNF layer, possibly alleviates the localized current density around the protrusion of the electrode.

### 3.2. Suppression of side reactions

The hydrophobic property of the PNF layer can effectively block direct contact between the electrode and the electrolyte, which is expected to suppress the HER and the generation of byproducts. Linear sweep voltammetry (LSV) was conducted to evaluate the HER reaction behavior of the PNF-Cu electrode. The Tafel curves measured in 2 M ZnSO<sub>4</sub> at a scan rate of 0.5 mV s<sup>-1</sup> show a more negative corrosion potential and lower current of PNF-Zn (Figure 2c) than those of the bare Cu electrode, suggesting that the PNF layer can effectively suppress the HER.

Additionally, to investigate the corrosion resistance property of PNF in the electrolyte, bare Zn foil and Zn foil electrospun with PNF (PNF-Zn) were immersed in 2 M ZnSO<sub>4</sub> electrolyte for 7 days, followed by surface analysis. Figure 2d shows that a number of byproducts are generated on the bare Zn surface, which is known as ZHS, such as

((Zn(OH)<sub>2</sub>)<sub>3</sub>(ZnSO<sub>4</sub>)(H<sub>2</sub>O)<sub>3</sub> or (Zn(OH)<sub>2</sub>)<sub>3</sub>(ZnSO<sub>4</sub>)(H<sub>2</sub>O)<sub>5</sub>.[35]. The ZHS formed on the electrode can deteriorate cell performance due to its insulating property and continuous water consumption [51]. However, in Figure 2e, some corrosion occurred, but it was confirmed that the pristine surface of Zn was maintained relatively well after removing the PNF layer from PNF-Zn. The FT-IR spectra and XRD data further confirm that the byproducts formed on the Zn surface are ZHS and that PNF has superior corrosion resistance, prohibiting ZHS formation on the surface of PNF-Zn (Figure 3f and S3). In FTIR spectra, the peaks related to H<sub>2</sub>O (O-H stretching vibrations and H<sub>2</sub>O bending vibrations) and SO<sub>4</sub> (S-O bending vibrations and O-S-O stretching vibrations) are significantly reduced with the PNF-Cu electrode. The XRD data in Figure S3 also showed the intensity of the ZHS-related peaks at 16.2, 24.4, and 32.7 ° are substantially suppressed in the PNF layer compared to the bare Zn [52].

### 3.3. Zn deposition morphology

After electrodeposition of 5 mAh cm<sup>-2</sup> Zn on the PNF-Cu electrode under various current densities, the PNF layer was carefully removed to observe the morphology of Zn deposition, and it was confirmed that Zn deposition occurred below the PNF layer (Figure S4 in SI).

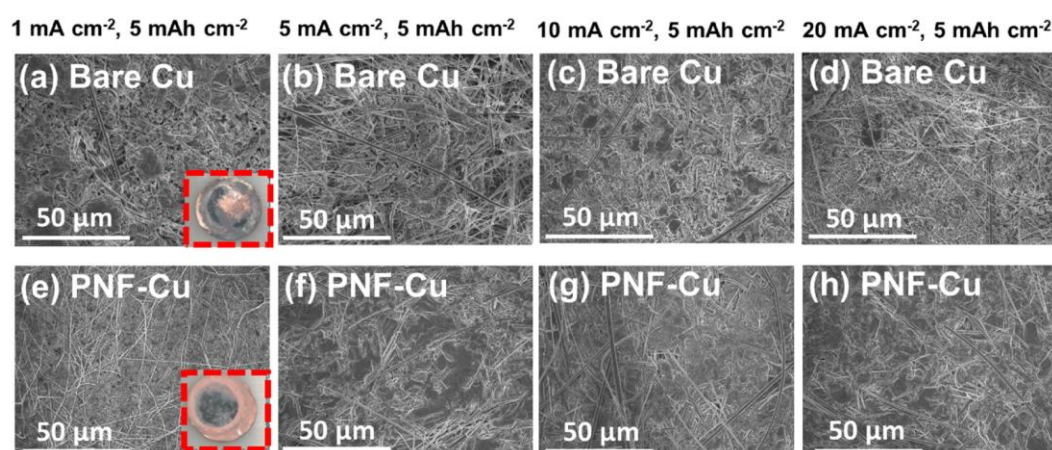


**Figure 3.** Top-view SEM images of Zn deposition morphology on (a-d) bare Cu electrode and (e-h) PNF-Cu under various current densities and fixed areal capacity of 5 mAh cm<sup>-2</sup>.

The SEM and digital images in Figure 3 and Figure S5 in the SI show a uniform and compact surface without dendrites with the PNF layer, indicating that the PNF layer effectively suppresses dendrite formation and induces uniform Zn deposition. In contrast, a non-uniform and loose deposition morphology is observed on the bare Cu electrodes. In particular, the difference in Zn deposition morphology between the Cu electrode and PNF-Cu electrode at a high current density (20 mA cm<sup>-2</sup>) is significant. On the surface of the Cu electrode, sharp dendrites are observed, while a smooth surface is observed on the PNF-Cu electrode. Considering that Zn is easily deposited at the initial nucleation site and protrusion grows, it can be inferred that PNF made the electric field uniform in the PNF-Cu electrode, leading to uniform Zn electrodeposition. To verify the effectiveness of the PNF layer, we constructed a Zn||Cu half cell with two glass fiber separators that have a fiber morphology similar to that of PNFs but have a higher thickness than that of PNFs and observed a Zn deposition morphology under 1 mA cm<sup>-2</sup> with a capacity of 5 mAh cm<sup>-2</sup> (Figure S6 in SI). The nonuniform Zn morphology is observed in the cell, as shown in Figure S7, and the result indicates that the PNF layer is not a simple mechanical barrier, and the uniform Zn deposition comes from the high polarity of the PNF layer.

### 3.4. Electrochemical properties of the half cells and symmetric cells

Zn||Cu and Zn||PNF-Cu half cells were constructed to evaluate the reversibility of Zn plating/stripping of the PNF-Cu electrode. The PNF-Cu electrode exhibits a high average Coulombic efficiency (CE) of 99.2% over 300 cycles and a stable cycling performance without a short circuit, while the Zn||Cu half-cell and Zn||Cu half-cell specimens using two separators show a short circuit from dendrite formation before the 300th cycle under  $1 \text{ mA cm}^{-2}$  with a capacity of  $1 \text{ mAh cm}^{-2}$  (Figure 4a, c, d, and Figure S8a). These results indicate that when Zn ions are electrodeposited on the Cu electrode surface, dendrites are formed by the localized current density around the tip. In contrast, in the case of the PNF-Cu electrode, the aligned molecular structure of the PNF layer can respond to the localized electric field, relax the localized current density, and inhibits dendrite formation, leading to reversible Zn plating/stripping. The PVDF-Cu electrode was also tested to examine the effect of the  $\beta$ -phase ratio on cell performance, and a short circuit occurred at approximately 160 cycles, demonstrating poor cycling stability compared to the PNF-Cu electrode (Figure S8b in SI) due to the fact that the fraction of the  $\beta$ -phase of PVDF nanofibers is approximately 10% lower than that of PNF, signifying the importance of the  $\beta$ -phase for performance improvement.

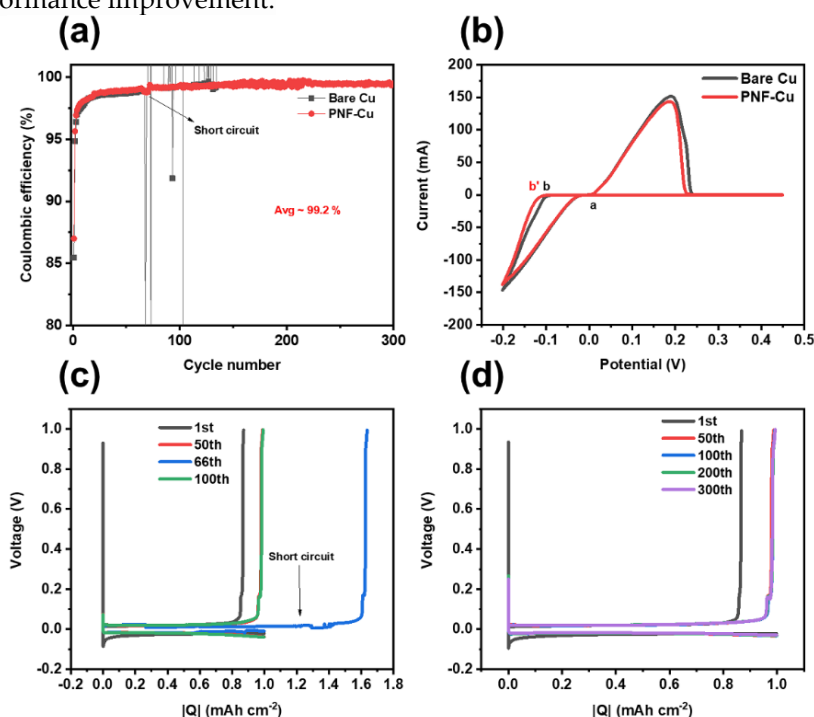


**Figure 4.** (a) Coulombic efficiency, (b) cyclic voltammetry, voltage profile of (c) Zn || Cu half cell, and (d) Zn || PNF-Cu half cell.

The cyclic voltammetry (CV) test was carried out with the Cu or PNF-Cu and Zn electrodes as working and counter electrodes, respectively (Figure 4b). This shows that the shape of the CV graph is well maintained after the introduction of the nanofiber layer, so the PNF layer remains stable during battery operation and does not affect the reversible Zn/Zn<sup>2+</sup> reaction. A crossover point (a) can be observed in the positive potential sweeping. The PNF-Cu electrode shows a slightly higher nucleation overpotential (a-b) than the bare Cu electrode (a-b') due to the hydrophobic nature of the PNF layer.

The electrochemical stability of the PNF-Cu anode was further investigated by galvanostatic cycling of the symmetric cell under diverse current densities (Figure 5). Before the cell assembly,  $5 \text{ mAh cm}^{-2}$  Zn was electrodeposited on the Cu electrode and the PNF-Cu electrode at a rate of  $1 \text{ mA cm}^{-2}$ . Under  $1\text{-}10 \text{ mA cm}^{-2}$ , the PNF-Cu shows stable plating/stripping cycles with a steady voltage-time profile but high overpotential derived from the hydrophobicity of the PNF layer. It is noticeable that at a current density of  $0.1 \text{ mA cm}^{-2}$ , the PNF-Cu symmetric cell shows a shorter cycle life than the cycle life of the

bare Cu symmetric cell. The shorter cycle life of the symmetric cell using Zn@PNF-Cu indicates that the low current density of  $0.1 \text{ mA cm}^{-2}$  is not sufficient to make oriented dipole moments along the external electric field.

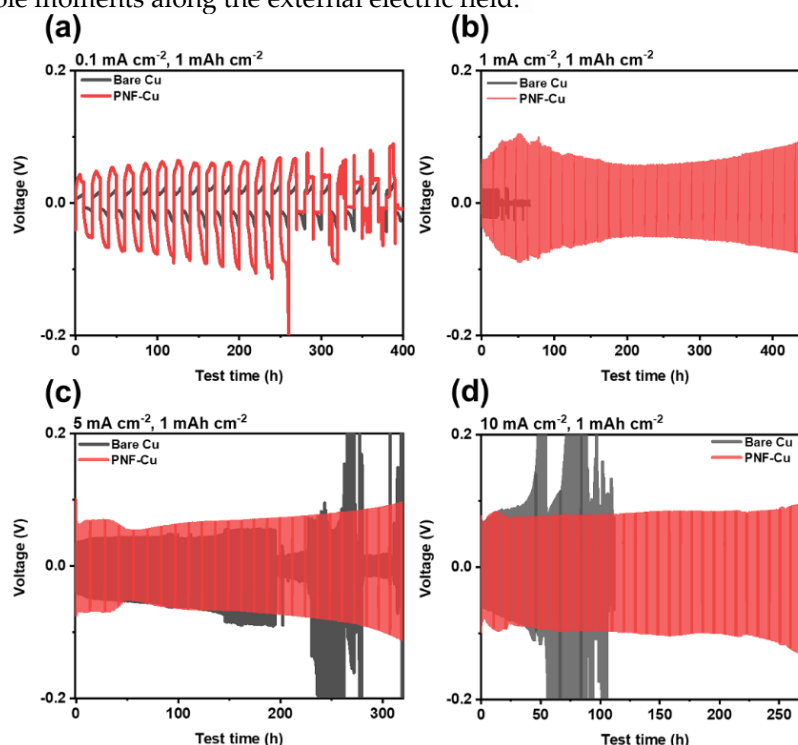


**Figure 5.** (a) Voltage–time curves of symmetric cells of zinc-deposited bare copper and P(VDF-TrFE) electrospun Cu at (a)  $0.1 \text{ mA cm}^{-2}$  (b)  $1 \text{ mA cm}^{-2}$  (c)  $5 \text{ mA cm}^{-2}$  (d)  $10 \text{ mA cm}^{-2}$ .

This result implies that a moderate current density is required to utilize the PNF layer, and further research to make PNF hydrophilic is required to utilize the PNF layer to reduce the overpotential of the cell. The voltage–time profiles in Figure 5a-d show that as the current density increases, the overpotential of the Zn@Cu symmetric cells during cycling dramatically increases due to nonuniform dendritic Zn growth. However, in the case of the Zn@PNF-Cu symmetric cell, it was confirmed that the increase in the overpotential by the current density is not significant compared to the Zn@Cu symmetric cell due to uniform Zn deposition, although it shows a larger overpotential than the Zn@Cu symmetric cell, ascribed to the hydrophobic nature of PNF (Figure 5a-d). As a result, at a high current density of  $10 \text{ mA cm}^{-2}$ , the Zn@PNF-Cu symmetric cell maintains a stable voltage profile over 250 hours, while Zn@Cu symmetric cells fail only after 40 hours with increasing voltage hysteresis. Thus, the results imply that the PNF layer can suppress dendrite formation for a longer time without short-circuiting under various current densities.

### 3.5. Full-cell test

To validate the practical use of the PNF-Cu electrode as an anode material for aqueous ZIBs, a full-cell performance test is conducted after pairing it with a  $\text{MnO}_2$  cathode. Figure 6a presents the charge–discharge profiles of the Zn@Cu cell. The voltage gap rapidly increases, and the capacity decreases as the cycle progresses. However, in the cell using the Zn@PNF-Cu electrode (Figure 6b), the increase in voltage gap and decrease in capacity during repeated cycling are restrained. At a current density of  $0.5 \text{ A g}^{-1}$ , the cell using the Zn@PNF-Cu electrode shows moderate capacity fading during cycling, delivering  $79.18 \text{ mAh g}^{-1}$  after 200 cycles, whereas the cell using the Zn@Cu electrode shows rapid capacity fading after 120 cycles, delivering only  $53.16 \text{ mAh g}^{-1}$  after 200 cycles (Figure 6c). This is because when a Zn@PNF-Cu electrode is used, reversible Zn plating/stripping occurs, and side reactions between the electrode interfaces can be curbed.



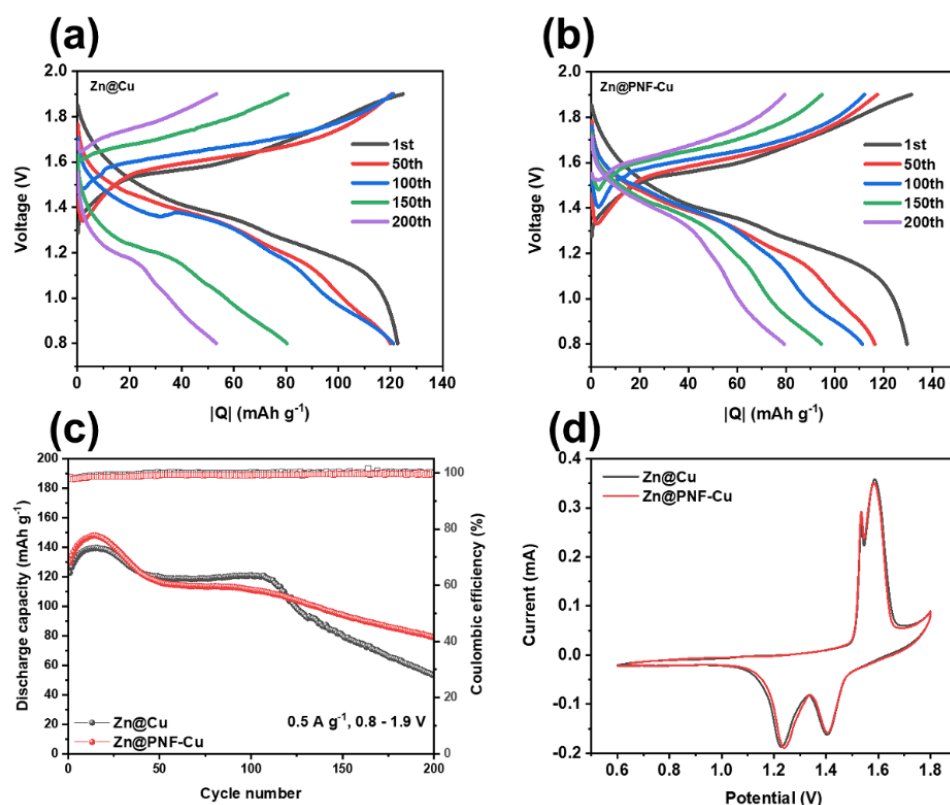


**Figure 6.** Zn-MnO<sub>2</sub> full-cell performance; charge and discharge curves of the cells using (a) Zn@Cu and (b) Zn@PNF-Cu; (c) cycling performance at 0.5 mA g<sup>-1</sup>; (d) CV curves at a scan rate of 0.1 mV s<sup>-1</sup>.

Additionally, the CE in the case of Zn@Cu often exceeds 100%, which seems to be due to a side reaction between the electrode and the electrolyte interface, and this phenomenon is not observed in the Zn@PNF-Cu electrode system. The CV curves are shown in Figure 6d, illustrating the high reversibility of the full cells. Both electrodes displayed the two characteristic redox peaks of MnO<sub>2</sub> ascribed to multiple phase conversions with similar peak currents and positions, confirming that the PNF layer on the anode does not affect the reversible electrochemical reactions of the MnO<sub>2</sub> cathode [52,53]. The performance of electrospun Zn@PNF-Cu anode is superior to many previous works, as summarized in Table S1, in SI. Some of the previous zinc anodes presented excellent cycling stability under low current density, whereas some anodes worked at higher current density, they could only deliver a limited number of cycles. These promising results verify the remarkable electrochemical performance and possible use in practical applications of the Zn@PNF-Cu electrode in ZIBs.

#### 4. Conclusions

In summary, we introduced electrospun PNF onto a Cu electrode to address the dendrite formation issue in ZIBs. We confirmed that a high proportion of  $\beta$ -crystalline phase was formed in PNFs through electrospinning followed by heat treatment. After the introduction of the PNF layer, the formation of dendrites was effectively suppressed by alleviating the local current density with its unique aligned molecular structure. Moreover, ascribed to its hydrophobic properties, the PNF layer can suppress the side reaction between the electrode and electrolyte. As a result, the PNF-Cu || Zn half-cell configuration achieved an average coulombic efficiency of 99.2% over 300 cycles. Additionally, the possibility of practical use was confirmed by maintaining cycling stability for 200 cycles at 0.5 A g<sup>-1</sup> when a full cell was constructed with the MnO<sub>2</sub> cathode. On the basis of the above results, we anticipate that the PNF-Cu electrode can provide a practical and meaningful approach to safe and highly efficient ZIBs.

**Supplementary Materials:** The voltage–time curves on Zn and Cu substrate; ionic resistivity measurement (Nyquist plots) of the bare Cu and electrospun Cu symmetric cells with the glass fiber as a separator; digital images of Zn deposition on the bare Cu and PNF-Cu; SEM images of Zn deposition morphology on bare Cu electrode and PNF-Cu under various current densities; cross-sectional SEM image of the glass fiber; SEM images of Zn deposition morphology of Zn||Cu cell using two glass fibers as a separator; coulombic efficiencies of long-term cycles for the Zn||Cu half cell using 2 separators and the Zn||PVDF-Cu half cell; comparison table for the cyclic performances of various modified Zn anode

**Acknowledgments:** This research was supported by the ‘2022 Joint Research Project of Institutes of Science and Technology’ and the Korea Institute of Energy Technology Evaluation and Planning (KETEP) and the Ministry of Trade, Industry & Energy (MOTIE) of the Republic of Korea (No. 20204010600340).

## References

- [1] Kim, J.-K.; Mueller, F.; Kim, H.; Jeong, S.; Park, J. -S.; Passerini, S.; Kim, Y. Eco-friendly Energy Storage System: Seawater and Ionic Liquid Electrolyte. *ChemSusChem*. **2016**, *9*, 42-49.
- [2] Alam, R.B.; Ahmad, M. H.; Islam, M. R. Bio-inspired gelatin/single-walled carbon nanotube nanocomposite for transient electrochemical energy storage: An approach towards eco-friendly and sustainable energy system. *Heliyon*. **2021**, *7*, e07468.
- [3] Chang, N.; Li, T.; Li, R.; Wang, S.; Yin, Y.; Zhang, H.; Li, X. An aqueous hybrid electrolyte for low-temperature zinc-based energy storage devices. *Energy Environ. Sci.* **2020**, *13*, 3527-3535.
- [4] Mensah-Darkwa, K.; Zequine, C.; Kahol, P. K.; Gupta, R. K. Supercapacitor Energy Storage Device Using Biowastes: A Sustainable Approach to Green Energy. *Sustainability* **2019**, *11*, 414.
- [5] Choi, J. W.; Aurbach, D. Promise and reality of post-lithium-ion batteries with high energy densities. *Nat. Rev. Mater.* **2016**, *1*, 16013.
- [6] Ogumi, Z.; Kostecki, R.; Guyomard, D.; Inaba, M. Lithium-Ion Batteries-The 25th Anniversary of Commercialization. *Interface mag.* **2016**, *25*, 65-65.
- [7] Yoshino, A. The Birth of the Lithium-Ion Battery. *Angew. Chem. Int. Ed.* **2012**, *51*, 5798-5800.
- [8] Liu, J.; Xu, C.; Chen, Z.; Ni, S.; Shen, Z. X. Progress in aqueous rechargeable batteries. *Green Energy Environ.* **2018**, *3*, 20-41.
- [9] Balakrishnan, P. G.; Ramesh, R.; Prem Kumar, T. Safety mechanisms in lithium-ion batteries. *J. Power Sources* **2006**, *155*, 401-414.
- [10] Chawla, N.; Bharti, N.; Singh, S. Recent Advances in Non-Flammable Electrolytes for Safer Lithium-Ion Batteries. *Batteries* **2019**, *5*, 19.
- [11] Wang, F.; Borodin, O.; Ding, M. S.; Gobet, M.; Vatamanu, J.; Fan, X.; Gao, T.; Eidson, N.; Liang, Y.; Sun, W.; Greenbaum, S.; Xu, K.; Wang, C. Hybrid Aqueous/Non-aqueous Electrolyte for Safe and High-Energy Li-Ion Batteries. *Joule* **2018**, *2*, 927-937.
- [12] Dou, Q.; Wang, Y.; Wang, A.; Ye, M.; Hou, R.; Lu, Y.; Su, L.; Shi, S.; Zhang, H.; Yan, X. Water in salt/ionic liquid” electrolyte for 2.8 V aqueous lithium-ion capacitor. *Sci. Bull.* **2020**, *65*, 1812-1822.
- [13] Ren, J.; Li, C.; Li, H.; Li, Z.; Liu, S.; Luo, B.; Wang, L. Realizing highly stable zinc-ion batteries via electrolyte engineering with adsorbed molecular protective layer. *Electrochim. Acta.* **2022**, *427*, 140876.
- [14] Sun, P.; Liu, W.; Yang, D.; Zhang, Y.; Xiong, W.; Li, S.; Chen, J.; Tian, J.; Zhang, L. Stable Zn anodes enabled by high-modulus agarose gel electrolyte with confined water molecule mobility. *Electrochim. Acta.* **2022**, *429*, 140985.
- [15] Hoang Huy, V. P.; Hieu, L. T.; Hur, J. Zn Metal Anodes for Zn-Ion Batteries in Mild Aqueous Electrolytes: Challenges and Strategies. *Nanomaterials* **2021**, *11*, 2746.
- [16] Yan, J.; Ang, E. H.; Yang, Y.; Zhang, Y.; Ye, M.; Du, W.; Li, C. C. High-Voltage Zinc-Ion Batteries: Design Strategies and Challenges. *Adv. Funct. Mater.* **2021**, *31*, 2010213.
- [17] Chen, D.; Lu, M.; Cai, D.; Yang, H.; Han, W. Recent advances in energy storage mechanism of aqueous zinc-ion batteries. *J. Energy Chem.* **2021**, *54*, 712-726.
- [18] Kim, E.; Choi, I.; Nam, K. W. Metal–organic framework for dendrite-free anodes in aqueous rechargeable zinc batteries. *Electrochim. Acta.* **2022**, *425*, 140648.

- [19] Yang, Q.; Li, Q.; Liu, Z.; Wang, D.; Guo, Y.; Li, X.; Tang, Y.; Li, H.; Dong, B.; Zhi, C. Dendrites in Zn-Based Batteries. *Adv. Mater.* **2020**, *48*, 2001854.
- [20] Kumar, S.; Yoon, H.; Park, H.; Park, G.; Suh, S.; Kim, H. -J. A dendrite-free anode for stable aqueous rechargeable zinc-ion batteries. *J. Ind. Eng. Chem.* **2022**, *108*, 321-327.
- [21] Liu, B.; Wang, S.; Wang, Z.; Lei, H.; Chen, Z.; Mai, W. Novel 3D Nanoporous Zn–Cu Alloy as Long-Life Anode toward High-Voltage Double Electrolyte Aqueous Zinc-Ion Batteries. *Small* **2020**, *16*, 2001323.
- [22] Li, B.; Xue, J.; Han, C.; Liu, N.; Ma, K.; Zhang, R.; Wu, X.; Dai, L.; Wang, L.; He, Z. A hafnium oxide-coated dendrite-free zinc anode for rechargeable aqueous zinc-ion batteries. *J. Colloid Interface Sci.* **2021**, *599*, 467-475.
- [23] Chen, P.; Yuan, X.; Xia, Y.; Zhang, Y.; Fu, L.; Liu, L.; Yu, N.; Huang, Q.; Wang, B.; Hu, X.; Wu, Y.; Ree, T. V. An Artificial Polyacrylonitrile Coating Layer Confining Zinc Dendrite Growth for Highly Reversible Aqueous Zinc-Based Batteries. *Adv. Sci.* **2021**, *8*, 2100309.
- [24] Jian, Q.; Wan, Y.; Sun, J.; Wu, M.; Zhao, T. A dendrite-free zinc anode for rechargeable aqueous batteries. *J. Mater. Chem.* **2020**, *8*, 20175-20184.
- [25] He, H.; Qin, H.; Wu, J.; Chen, X.; Huang, R.; Shen, F.; Wu, Z.; Chen, G.; Yin, S.; Liu, J. Engineering interfacial layers to enable Zn metal anodes for aqueous zinc-ion batteries. *Energy Stor. Mater.* **2021**, *43*, 317-336.
- [26] Pusty, M.; Shirage, P. M. Insights and perspectives on graphene-PVDF based nanocomposite materials for harvesting mechanical energy. *J. Alloys Compd.* **2022**, *904*, 164060.
- [27] Yu, Y.; Shao, W.; Zhong, J.; Ye, H.; Yang, L.; Zhen, L. Tuning the Energy Storage Efficiency in PVDF Nanocomposites Incorporated with Crumpled Core–Shell BaTiO<sub>3</sub>@Graphene Oxide Nanoparticles. *ACS Appl. Energy Mater.* **2021**, *4*, 9553-9562.
- [28] Zhang, M.; Tan, S.; Xiong, J.; Chen, C.; Zhang, Y.; Wei, X.; Zhang, Z. Tailoring Dielectric and Energy Storage Performance of PVDF-Based Relaxor Ferroelectrics with Hydrogen Bonds. *ACS Appl. Energy Mater.* **2021**, *4*, 8454-8464.
- [29] Yi, Z.; Wang, Z.; Nian, W.; Wang, T.; Chen, H.; Cheng, Z. High Energy Storage Density of Sandwich-Structured Na<sub>0.5</sub>Bi<sub>0.5</sub>TiO<sub>3</sub>/PVDF Nanocomposites Enhanced by Optimizing the Dimensions of Fillers. *ACS Appl. Energy Mater.* **2021**, *4*, 13528-13537.
- [30] Shepelin, N. A.; Sherrell, P. C.; Skountzos, E. N.; Goudeli, E.; Zhang, J.; Lussini, V. C.; Imtiaz, B.; Usman, K. A. S.; Dicinosk, G. W.; Shapter, J. G.; Razal, J. M.; Ellis, A. V. Interfacial piezoelectric polarization locking in printable Ti<sub>3</sub>C<sub>2</sub>T<sub>x</sub> MXene-fluoropolymer composites. *Nat. Commun.* **2021**, *12*, 3171.
- [31] Fortunato, M.; Cavallini, D.; Bellis, G. D.; Marra, F. A. Tamburrano, F. Sarto, M. S. Sarto, Phase Inversion in PVDF Films with Enhanced Piezoresponse Through Spin-Coating and Quenching. *Polymers* **2019**, *11*, 1096.
- [32] Kim, M.; Lee, S.; Kim, Y.-I. Solvent-controlled crystalline beta-phase formation in electrospun P(VDF-TrFE) fibers for enhanced piezoelectric energy harvesting. *APL Mater.* **2020**, *8*, 071109.
- [33] Song, W. -J.; Joo, S. H.; Kim, D. H.; Hwang, C.; Jung, G. Y.; Bae, S.; Son, Y.; Cho, J.; Song, H. -K.; Kwak, S. K.; Park, S.; Kang, S. -J. Significance of ferroelectric polarization in poly (vinylidene difluoride) binder for high-rate Li-ion diffusion. *Nano Energy* **2017**, *32*, 255-262.
- [34] Hwang, C.; Song, W. -J.; Song, G.; Wu, Y.; Lee, S.; Son, H. B.; Kim, A. J.; Liu, N.; Park, S.; Song, H. -K. A Three-Dimensional Nano-web Scaffold of Ferroelectric Beta-PVDF Fibers for Lithium Metal Plating and Stripping. *ACS Appl. Mater. Interfaces* **2020**, *12*, 29235-29241.
- [35] Wang, Y.; Liu, Y.; Wang, H.; Dou, S.; Gan, W.; Ci, L.; Huang, Y.; Yuan, Q. MOF-based ionic sieve interphase for regulated Zn<sup>2+</sup> flux toward dendrite-free aqueous zinc-ion batteries. *J. Mater. Chem.* **2022**, *10*, 4366-4375.
- [36] Zhang, C.; Zhang, T.; Feng, M.; Cui, Y.; Zhang, T.; Zhang, Y.; Feng, Y.; Zhang, Y.; Chi, Q.; Liu, X. Significantly Improved Energy Storage Performance of PVDF Ferroelectric Films by Blending PMMA and Filling PCBM. *ACS Sustain. Chem. Eng.* **2021**, *9*, 16291-16303.
- [37] Mayeen, A.; Kala, M. S.; Sunija, S.; Rouxel, D.; Bhowmik, R. N.; Thomas, S.; Kalarikkal, N. Flexible dopamine-functionalized BaTiO<sub>3</sub>/BaTiZrO<sub>3</sub>/BaZrO<sub>3</sub>-PVDF ferroelectric nanofibers for electrical energy storage. *J. Alloys Compd.* **2020**, *837*, 155492.

- [38] Wang, Y.; Guo, T.; Yin, J.; Tian, Z.; Ma, Y.; Liu, Z.; Zhu, Y.; Alshareef, H. N. Controlled Deposition of Zinc-Metal Anodes via Selectively Polarized Ferroelectric Polymers. *Adv. Mater.* **2020**, *34*, 2106937.
- [39] Mai, M.; Ke, S.; Lin, P.; Zeng, X. Ferroelectric Polymer Thin Films for Organic Electronics. *J. Nanomater.* **2015**, 812538.
- [40] Abrha, L. H.; Nikodimos, Y.; Weldeyohannes, H. H.; Hagos, T. T.; Wang, D. -Y.; Huang, C. -J.; Jiang, S. -K.; Wu, S. -H.; Su, W. -N.; Tsai, M. -C.; Hwang, B. J. Effects of a Thermally Electrochemically Activated  $\beta$ -PVDF Fiber on Suppression of Li Dendrite Growth for Anode-Free Batteries. *ACS Appl. Energy Mater.* **2021**, *4*, 3240-3248.
- [41] Li, C.; Qiu, M.; Li, R.; Li, X.; Wang, M.; He, J.; Lin, G.; Xiao, L.; Qian, Q.; Chen, Q.; Wu, J.; Li, X.; Mai, Y.; Chen, Y. Electrospinning Engineering Enables High-Performance Sodium-Ion Batteries. *Adv. Fiber Mater.* **2022**, *4*, 43-65.
- [42] Li, R.; Wu, J.; He, J.; Li, X.; Mai, Y.; Chen, Y.; Li, X. Embedding amorphous SnS in electrospun porous carbon nanofibers for efficient potassium storage with ultralong cycle life. *Compos. B. Eng.* **2022**, *243*, 110132.
- [43] Li, X.; Chen, W.; Qian, Q.; Huang, H.; Chen, Y.; Wang, Z.; Chen, Q.; Yang, J.; Li, J.; Mai, Y. Electrospinning-Based Strategies for Battery Materials. *Adv. Energy Mater.* **2021**, *11*, 2000845.
- [44] Xie, S.; Li, Y.; Li, X.; Zhou, Y.; Dang, Z.; Rong, J.; Dong, L. Stable Zinc Anodes Enabled by Zincophilic Cu Nanowire Networks. *Nanomicro Lett* **2021**, *14*, 39.
- [45] Zhou, L.; Yang, F.; Zeng, S.; Gao, X.; Liu, X.; Cao, X.; Yu, P.; Lu, X. Zincophilic Cu Sites Induce Dendrite-Free Zn Anodes for Robust Alkaline/Neutral Aqueous Batteries. *Adv. Funct. Mater.* **2022**, *32*, 2110829.
- [46] Xie, C.; Li, Y.; Wang, Q.; D. Sun, D.; Tang, T.; Wang, H. Issues and solutions toward zinc anode in aqueous zinc-ion batteries: A mini review. *Carbon energy* **2020**, *2*, 540-560.
- [47] Ruan, L.; Yao, X.; Chang, Y.; Zhou, L.; Qin, G.; Zhang, X. Properties and Applications of the  $\beta$  Phase Poly(vinylidene fluoride). *Polymers* **2018**, *10*, 228.
- [48] Sathiyaraju, M.; Ramesh, T.; Effect of annealing treatment on PVDF nanofibers for mechanical energy harvesting applications. *Mater. Res. Express* **2019**, *6*, 105366.
- [49] Poudel, A.; Fernandez, M. A.; Tofail, S. A. M.; Biggs, M. J. P. Boron Nitride Nanotube Addition Enhances the Crystallinity and Cytocompatibility of PVDF-TrFE. *Front. Chem.* **2019**, *7*, 364.
- [50] Wu, Y.; Du, X.; Gao, R.; Li, J.; Li, W.; Yu, H.; Jiang, Z.; Wang, Z.; Tai, H. Self-Polarization of PVDF Film Triggered by Hydrophilic Treatment for Pyroelectric Sensor with Ultra-Low Piezoelectric Noise. *Nanoscale Res. Lett.* **2019**, *14*, 72
- [51] Zhang, Q.; Yang, Z.; Ji, H.; Zeng, X.; Tang, Y.; Sun, D.; Wang, H. Issues and rational design of aqueous electrolyte for Zn-ion batteries. *SusMat* **2021**, *1*, 432-447.
- [52] Yang, J.; Cao, J.; Peng, Y.; Yang, W.; Barg, S.; Liu, Z.; Kinloch, I.A.; Bissett, M.A.; Dryfe, R.A.W. Unravelling the Mechanism of Rechargeable Aqueous Zn-MnO<sub>2</sub> Batteries: Implementation of Charging Process by Electrodeposition of MnO<sub>2</sub>. *ChemSusChem* **2020**, *13*, 4103-4110.
- [53] Li, L.; Hoang, T. K. A.; Zhi, J.; Han, M.; Li, S.; Chen, P. Functioning Mechanism of the Secondary Aqueous Zn- $\beta$ -MnO<sub>2</sub> Battery. *ACS Appl. Mater. Interfaces* **2020**, *12*, 12834-12846.
- [54] Liu, W.; Zhang, X.; Huang, Y.; Jiang, B.; Chang, Z.; Xu, C.; Kang, F.  $\beta$ -MnO<sub>2</sub> with proton conversion mechanism in rechargeable zinc ion battery. *J. Energy Chem.* **2021**, *56*, 365-373.